Stiffness matrices for fluid and anisotropic soil layers with applications in soil dynamics

Joonsang Park*, Amir M. Kaynia

Norwegian Geotechnical Institute (NGI), Oslo, Norway

ABSTRACT

In this study, we introduce and discuss features and improvements of the well-established stiffness matrix method that is used in simulation of wave propagation in layered media. More specifically, we present stiffness matrices for an acoustic layer and a vertically transverse isotropic (VTI) viscoelastic soil layer. Combining these stiffness matrices enables a straightforward technique for modeling of acousto-elastic wave propagation in layered infinite media. In addition, we propose a technique to simulate discontinuity seismic sources, which was not used earlier in the context of the stiffness matrix method. Finally, we propose a framework to derive a key parameter of the absorbing boundary domain technique Perfectly Matched Layer (PML). Numerical examples are presented in order to help understanding the features and improvements discussed in the study from the fields of geophysics and soil dynamics. It is believed that the features and improvements discussed herein will make the application of the stiffness matrix method even wider and more flexible.

1. Introduction

The stiffness matrix method is a well-developed approach for simulating wave propagation in layered media, and has been successfully applied to various problems during the last decades (e.g. [1–3] and [4]). The method describes the wave motion in a layered medium in terms of symmetric and banded matrices and with straightforward and efficient solution procedure, producing the dynamic responses simultaneously at all layer interfaces and in all directions. The method has later been extended to acoustic layers ([5,6]). The discrete version of the stiffness matrix solution, called Thin-Layer Method (TLM), has also been developed and applied to various problems ([7–9]). Recently, TLM has been combined with the so-called Perfectly Matched Layer method (PML) that enables calculation of wave motion in infinite domains [10]. Despite these extensions, there are still features and improvements of the stiffness matrix method that could advance the use of the method in theoretical and applied problems. The present study introduces and discusses some of those features, including

- Vertically transverse isotropic (VTI) soil layer stiffness
- Discontinuity seismic sources
- Derivation of PML parameters

For completeness, first we present the acoustic layer stiffness matrices in forms that can be used in offshore or fluid-soil-coupled applications (e.g. seismic wave in the ocean environment). We introduce three different formulations in terms of vertical displacement, velocity potential and pressure. Each formulation has its own advantages and disadvantages. For example, the second and third formulations make it straightforward to implement the so-called air-gun source that is used as explosive acoustic source in offshore seismic surveys. This is because the air volume injected by the air-gun is explicitly defined in the two formulations, which are shown later. On the other hand, the first formulation is more suitable for applying vertical disk load on seabed or within water column, because the disk load can be represented by a term that can be set directly in the matrix equations. It is also shown that the three solutions are interrelated such that one can be derived from the other two through relevant constitutive laws. Next, the soil stiffness matrices for the vertically transverse isotropic (VTI) layers are derived for both P-SV (in-plane) and SH (antiplane) wave modes. It is shown that the structure of the VTI soil layer stiffness matrices is identical to that of the isotropic soil layer, except that the parameters have different definitions and include the anisotropy factors (a and b). Indeed, the stiffness matrix for the isotropic case can be recovered by setting the anisotropy factors equal to 1. This allows straightforward extension of existing numerical tools based on stiffness matrices in isotropic soil to anisotropic soil. The derived stiffness matrices are used to compute the impedance matrices of square

---

* Corresponding author.
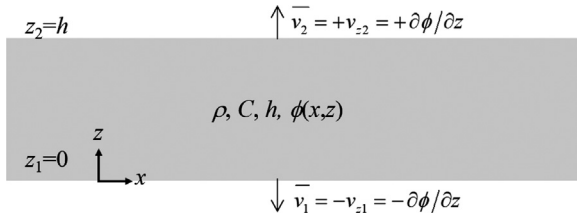*E-mail address:* joonsang.park@ngi.no (J. Park).

Fig. 1. Acoustic layer of mass density ρ, wave velocity C and thickness h whose motion is expressed by the particle velocity potential ϕ. Note that two flux boundary conditions at $z = 0$ and h are given in terms of volume change $\bar{v}$.

foundations on anisotropic soil media and the results are compared with their isotropic counterparts to highlight the effect of anisotropy on the foundation impedances. Further, in order to solve the case of injected (air or fluid) volume or dislocation/slip at the interface of two layers, we formulate a technique to implement displacement discontinuity into the stiffness matrix method. This technique enables the stiffness matrix method to simulate the wave fields generated by e.g. an air-gun source or dislocation seismic sources. Finally, by means of the continuum stiffness matrices we derive the key parameter of PML (i.e. PML thickness, h_{PML}) that can be used in discrete numerical approaches, for example, in TLM, Finite Element Method (FEM) and Finite Difference Method (FDM).

2. Stiffness matrices for fluid and anisotropic soil layers

2.1. Acoustic layer

Fig. 1 shows schematically an acoustic layer of thickness h. Wave motion in an acoustic layer can be described with different equations. In this study, we have chosen the particle velocity potential (ϕ). The governing equation in the space-frequency domain has then the following form:

$$\nabla^2 \phi + \frac{\omega^2}{C^2}\phi = 0 \tag{1}$$

where ∇ is the Laplacian operator, ϕ is the velocity potential, ω is the angular frequency (in radian/s), and C is the wave velocity in the acoustic layer.

The velocity potential (ϕ) and the vertical velocity ($v_z = \partial\phi/\partial z$) in the wavenumber-frequency domain can be given in matrix forms as

$$\begin{Bmatrix} \phi \\ v_z \end{Bmatrix} = \begin{Bmatrix} e^{\beta z} & e^{-\beta z} \\ \beta e^{\beta z} & -\beta e^{-\beta z} \end{Bmatrix} \begin{Bmatrix} A \\ B \end{Bmatrix} \tag{2}$$

where A and B are unknown constants to be determined for each acoustic layer, $\beta = \sqrt{k^2 - \omega^2/C^2}$ is vertical direction wavenumber in the acoustic layer, and k is the radial (or horizontal) direction wavenumber. Note that hereby Fourier (for plane wave) or Hankel (for cylindrical wave) transformation from the spatial to wavenumber domain is already applied, and the wavenumber k replaces all the spatial derivatives with respect to the horizontal (or radial) coordinate. For an acoustic layer of finite thickness h, we can express explicitly the two quantities of the velocity potential and the vertical velocity on the top and bottom interfaces by setting $z = h$ and $z = 0$, resulting in the following two matrix equations.

$$\begin{Bmatrix} \phi_2 \\ v_{z2} \end{Bmatrix} = \begin{Bmatrix} e^{\beta h} & e^{-\beta h} \\ \beta e^{\beta h} & -\beta e^{-\beta h} \end{Bmatrix} \begin{Bmatrix} A \\ B \end{Bmatrix} \tag{3}$$

$$\begin{Bmatrix} \phi_1 \\ v_{z1} \end{Bmatrix} = \begin{Bmatrix} 1 & 1 \\ \beta & -\beta \end{Bmatrix} \begin{Bmatrix} A \\ B \end{Bmatrix} \tag{4}$$

Subscripts 1 and 2 indicate, respectively, the quantities on the bottom and top interfaces. By removing the unknown constant vector $\{A, B\}^T$ from the two matrix equations, we can obtain the following direct-relationship between the top and bottom interfaces (i.e. at $z = h$ and $z = 0$) in terms of the velocity potential and the vertical velocity given below

$$\begin{Bmatrix} \phi_2 \\ v_{z2} \end{Bmatrix} = \frac{1}{\beta} \begin{Bmatrix} \beta\cosh\beta h & \sinh\beta h \\ \beta^2\sinh\beta h & \beta\cosh\beta h \end{Bmatrix} \begin{Bmatrix} \phi_1 \\ v_{z1} \end{Bmatrix} \tag{5}$$

The equations can be rearranged further as

$$\begin{Bmatrix} v_{z1} \\ v_{z2} \end{Bmatrix} = \frac{\beta}{\sinh\beta h} \begin{Bmatrix} -\cosh\beta h & 1 \\ -1 & \cosh\beta h \end{Bmatrix} \begin{Bmatrix} \phi_1 \\ \phi_2 \end{Bmatrix} \tag{6}$$

In the context of the layer stiffness matrix method, we need to consider the volume change ($\bar{v}$) as the flux condition at an interface, representing the injected volume via, for example, air-gun source at the interface. In this way, we can easily assemble the layer stiffness matrix in the sense of the finite element method. For this, we need to consider the following relationships:

$$\bar{v}_1 = -v_{z1} \tag{7}$$

$$\bar{v}_2 = v_{z2} \tag{8}$$

The reason for the negative sign in the relationship for the bottom interface (Eq. (7)) is that the volume change is defined positive as it increases, which corresponds to the negative vertical velocity at the bottom interface. Eq. (6) can then be re-written as

$$\frac{\beta}{\sinh\beta h} \begin{Bmatrix} \cosh\beta h & -1 \\ -1 & \cosh\beta h \end{Bmatrix} \begin{Bmatrix} \phi_1 \\ \phi_2 \end{Bmatrix} = \begin{Bmatrix} \bar{v}_1 \\ \bar{v}_2 \end{Bmatrix} \tag{9}$$

which gives the symmetric acoustic layer stiffness matrix in terms of the velocity potential. Furthermore, the velocity potential can be converted into pressure according to the following constitutive law:

$$p = -i\omega\rho\phi \tag{10}$$

By applying this, we can transform the stiffness matrix in Eq. (9) into the following form in terms of pressure.

$$\frac{i\beta}{\rho\omega\sinh\beta h} \begin{Bmatrix} \cosh\beta h & -1 \\ -1 & \cosh\beta h \end{Bmatrix} \begin{Bmatrix} p_1 \\ p_2 \end{Bmatrix} = \begin{Bmatrix} \bar{v}_1 \\ \bar{v}_2 \end{Bmatrix} \tag{11}$$

In addition, we can also express the volume change ($\bar{v}$) in terms of the vertical displacement (u_z), and the pressure (p) in terms of the normal traction (σ_z) at the interface. For this, we use a set of constitutive laws of $\bar{v}_1 = -i\omega u_{z1}$, $\bar{v}_2 = i\omega u_{z2}$, $p_1 = -\sigma_{z1}$ and $p_2 = \sigma_{z2}$. Note that we need to impose the negative sign for the bottom interface. Then, we obtain the following stiffness matrix in terms of the vertical displacements.

$$\frac{\rho\omega^2}{\beta\sinh\beta h} \begin{Bmatrix} \cosh\beta h & -1 \\ -1 & \cosh\beta h \end{Bmatrix} \begin{Bmatrix} u_{z1} \\ u_{z2} \end{Bmatrix} = \begin{Bmatrix} \sigma_{z1} \\ \sigma_{z2} \end{Bmatrix} \tag{12}$$

As shown in Eqs. (9), (11) and (12), three versions for the acoustic layer stiffness matrix are available and are related to each other via the appropriate constitutive laws. It should be noted that the version with the vertical displacement (Eq. (12)) is in a form to be readily assembled with the soil layer stiffness matrix in the finite element sense without any additional condition to satisfy. On the other hand, the other two versions in Eqs. (9) and (11), with velocity potential and pressure, respectively, require additional interface conditions to satisfy. Such conditions are the flux continuity at interfaces, as given below in Eqs.

(13)–(16), and can be found in the literature (e.g. [8]).

For the velocity-potential acoustic layer stiffness:

$$\bar{v} = \pm i\omega u_z \tag{13}$$

$$\sigma_z = \pm i\omega\rho\phi \tag{14}$$

For the pressure acoustic layer stiffness:

$$\bar{v} = \pm i\omega u_z \tag{15}$$

$$\sigma_z = \pm p \tag{16}$$

2.2. Anisotropic soil layer

In this section, we present the layer stiffness matrices for a vertically transverse isotropic (VTI) soil layer whose anisotropy follows the principal coordinate directions. The procedure for the derivation of the VTI layer stiffness matrices is similar to that for the isotropic soil case [1]. Therefore, we skip presentation of most of the details of the derivation. Instead, we show the final result, which is constructed in such a way that the VTI layer stiffness matrices look similar in form to the isotropic layer stiffness matrices presented in [1]. As shown later in this section, the effect of transverse isotropy is accounted for with the help of two anisotropy factors a and b in the stiffness matrices.

In the elasticity theory, a VTI medium can be described by the stress-strain constitutive law in cylindrical coordinate system (r,θ,z), as given by:

$$\begin{pmatrix} \sigma_r \\ \sigma_\theta \\ \sigma_z \\ \tau_{\theta z} \\ \tau_{rz} \\ \tau_{r\theta} \end{pmatrix} = \begin{pmatrix} \lambda + 2G & \lambda & \lambda_t & 0 & 0 & 0 \\ \lambda & \lambda + 2G & \lambda_t & 0 & 0 & 0 \\ \lambda_t & \lambda_t & \lambda_t + 2G_t & 0 & 0 & 0 \\ 0 & 0 & 0 & G_t & 0 & 0 \\ 0 & 0 & 0 & 0 & G_t & 0 \\ 0 & 0 & 0 & 0 & 0 & G \end{pmatrix} \begin{pmatrix} \varepsilon_r \\ \varepsilon_\theta \\ \varepsilon_z \\ \gamma_{\theta z} \\ \gamma_{rz} \\ \gamma_{r\theta} \end{pmatrix} \tag{17}$$

where λ_t and G_t are the complex *Lamé* constants that are related to wave motion propagating in the vertical direction (z), and λ and G are related to wave propagation in the two horizontal directions (r,θ). These parameters incorporate linear hysteretic damping through the classical complex variable formalism. The associated wave velocities can be expressed as

$$C_p = \sqrt{\frac{\lambda + 2G}{\rho}} \tag{18a}$$

$$C_s = \sqrt{\frac{G}{\rho}} \tag{18b}$$

$$C_{pt} = \sqrt{\frac{\lambda_t + 2G_t}{\rho}} \tag{18c}$$

$$C_{st} = \sqrt{\frac{G_t}{\rho}} \tag{18d}$$

Wherein ρ is the mass density; C_p and C_s are the P- and S-wave velocities in *x-y* plane (i.e. along the horizontal direction); C_{pt} and C_{st} are the corresponding velocities in the vertical direction. In addition, we introduce the following three parameters that define the ratios between these wave velocities.

$$\alpha = \frac{C_{pt}}{C_{st}} \tag{19a}$$

$$a = \frac{C_p}{C_{pt}} \tag{19b}$$

$$b = \frac{C_s}{C_{st}} \tag{19c}$$

By applying the compatibility relationship between strain and displacement and inserting the stress-strain relationship into the momentum equilibrium equation, we can derive the frequency-domain wave equation for the VTI medium in cylindrical coordinate system as

$$\begin{aligned} &\left[\begin{Bmatrix} \lambda + 2G & 0 & 0 \\ 0 & G & 0 \\ 0 & 0 & G_t \end{Bmatrix} \frac{\partial^2}{\partial r^2} + \begin{Bmatrix} G & 0 & 0 \\ 0 & \lambda + 2G & 0 \\ 0 & 0 & G_t \end{Bmatrix} \frac{1}{r^2}\frac{\partial^2}{\partial \theta^2} \right. \\ &+ \begin{Bmatrix} G_t & 0 & 0 \\ 0 & G_t & 0 \\ 0 & 0 & \lambda_t + 2G_t \end{Bmatrix} \frac{\partial^2}{\partial z^2} + \begin{Bmatrix} 0 & \lambda + G & 0 \\ \lambda + G & 0 & 0 \\ 0 & 0 & 0 \end{Bmatrix} \frac{1}{r}\frac{\partial^2}{\partial r\partial \theta} \\ &+ \begin{Bmatrix} 0 & 0 & \lambda_t + G_t \\ 0 & 0 & 0 \\ \lambda_t + G_t & 0 & 0 \end{Bmatrix} \frac{\partial^2}{\partial r\partial z} + \begin{Bmatrix} 0 & 0 & 0 \\ 0 & 0 & \lambda_t + G_t \\ 0 & \lambda_t + G_t & 0 \end{Bmatrix} \frac{1}{r}\frac{\partial^2}{\partial \theta \partial z} \\ &+ \begin{Bmatrix} \lambda + 2G & 0 & 0 \\ 0 & G & 0 \\ 0 & 0 & G_t \end{Bmatrix} \frac{1}{r}\frac{\partial}{\partial r} + \begin{Bmatrix} 0 & -(\lambda + 3G) & 0 \\ \lambda + 3G & 0 & 0 \\ 0 & 0 & 0 \end{Bmatrix} \frac{1}{r^2}\frac{\partial}{\partial \theta} \\ &+ \left. \begin{Bmatrix} 0 & 0 & 0 \\ 0 & 0 & 0 \\ \lambda_t + G_t & 0 & 0 \end{Bmatrix} \frac{1}{r}\frac{\partial}{\partial z} - \begin{Bmatrix} \lambda + 2G & 0 & 0 \\ 0 & G & 0 \\ 0 & 0 & 0 \end{Bmatrix} \frac{1}{r^2} \right] \begin{Bmatrix} u \\ v \\ w \end{Bmatrix} + \begin{Bmatrix} b_r \\ b_\theta \\ b_z \end{Bmatrix} \\ &= -\rho\omega^2 \begin{Bmatrix} u \\ v \\ w \end{Bmatrix} \end{aligned} \tag{20}$$

where u, v and w are the displacement components along r, θ and z directions, respectively; and b_r, b_θ and b_z are the body forces in these directions. Following [1], the wave equation above can be solved by the separation of variables, where the displacement components are expressed as in Eq. (21) by:

$$\begin{Bmatrix} u(r, \theta, z) \\ v(r, \theta, z) \\ w(r, \theta, z) \end{Bmatrix} = \begin{Bmatrix} \cos n\theta & 0 & 0 \\ 0 & -\sin n\theta & 0 \\ 0 & 0 & \cos n\theta \end{Bmatrix} \begin{Bmatrix} \frac{dJ_n}{d(kr)} & \frac{n}{kr}J_n & 0 \\ \frac{n}{kr}J_n & \frac{dJ_n}{d(kr)} & 0 \\ 0 & 0 & -J_n \end{Bmatrix} \begin{Bmatrix} U(z) \\ V(z) \\ W(z) \end{Bmatrix} \tag{21}$$

In this equation, n is the azimuthal direction wavenumber (dimensionless integer); $J_n = J_n(kr)$ are the n-th order cylindrical functions of first, second or third kind (i.e. Bessel, Neumann, or Hankel functions, respectively); k is the radial-direction wavenumber; $U(z)$, $V(z)$, $W(z)$ are the z-direction dependencies (or vertical profiles) of the displacement modes. Note that $U(z)$ and $W(z)$ are related to the P-SV wave mode and $V(z)$ to the SH wave mode. The P-SV and SH wave modes of the VTI medium are completely decoupled from each other, as in the isotropic medium. The choice of n depends on the source characteristics along the azimuthal direction. For example, a vertical point load requires only $n = 0$ (i.e. no variation along θ), while a horizontal point load requires $n = 1$. However, if the source variation along θ-direction is more complex, the response should be obtained with the help of Fourier series and including as many n as needed until the sum is converged. The middle 3×3 matrix term on the right hand side in Eq. (21) is a standard form resulting from the solution by the separation of variables applied in the context of cylindrical coordinate system.

First, the 4×4 stiffness matrix for a VTI soil layer subjected to P-SV wave motion is given in the following in the same form as for the isotropic stiffness matrix presented in [1], except that the involved parameters are defined by different formula due to the soil anisotropy (See Eq. (26)).

$$\mathbf{K} = 2kG_t \begin{Bmatrix} \mathbf{K}_{11} & \mathbf{K}_{12} \\ \mathbf{K}_{21} & \mathbf{K}_{22} \end{Bmatrix} \tag{22}$$

$$\mathbf{K}_{11} = \frac{(\bar{k}_{z1}/\gamma_1 - \bar{k}_{z2}/\gamma_2)}{2D_t} \left\{ \begin{array}{cc} \gamma_2\left(C_1S_2 - \frac{\gamma_1}{\gamma_2}C_2S_1\right) & -\left[(1 - C_1C_2) + \frac{\gamma_1}{\gamma_2}S_1S_2\right] \\ -\left[(1 - C_1C_2) + \frac{\gamma_1}{\gamma_2}S_1S_2\right] & \frac{1}{\gamma_1}\left(C_2S_1 - \frac{\gamma_1}{\gamma_2}C_1S_2\right) \end{array} \right\}$$

$$-\frac{1}{2}(1 + \bar{k}_{z2}/\gamma_2)\begin{Bmatrix} 0 & 1 \\ 1 & 0 \end{Bmatrix} \mathbf{K}_{12} = \frac{(\bar{k}_{z1}/\gamma_1 - \bar{k}_{z2}/\gamma_2)}{2D_t} \left\{ \begin{array}{cc} \gamma_2\left(\frac{\gamma_1}{\gamma_2}S_1 - S_2\right) & -(C_1 - C_2) \\ (C_1 - C_2) & \frac{1}{\gamma_1}\left(\frac{\gamma_1}{\gamma_2}S_2 - S_1\right) \end{array} \right\}$$

$$= \mathbf{K}_{21}^T \mathbf{K}_{22} = \frac{(\bar{k}_{z1}/\gamma_1 - \bar{k}_{z2}/\gamma_2)}{2D_t} \left\{ \begin{array}{cc} \gamma_2\left(C_1S_2 - \frac{\gamma_1}{\gamma_2}C_2S_1\right) & \left[(1 - C_1C_2) + \frac{\gamma_1}{\gamma_2}S_1S_2\right] \\ \left[(1 - C_1C_2) + \frac{\gamma_1}{\gamma_2}S_1S_2\right] & \frac{1}{\gamma_1}\left(C_2S_1 - \frac{\gamma_1}{\gamma_2}C_1S_2\right) \end{array} \right\}$$

$$+ \frac{1}{2}(1 + \bar{k}_{z2}/\gamma_2)\begin{Bmatrix} 0 & 1 \\ 1 & 0 \end{Bmatrix} \tag{23}$$

The 2×2 stiffness matrix for a VTI lower ($z < 0$) half-space subjected to P-SV wave is also derived and expressed as

$$\mathbf{K}_{half} = 2kG_t\left[\frac{(\bar{k}_{z1}/\gamma_1 - \bar{k}_{z2}/\gamma_2)}{2(1 - \gamma_1/\gamma_2)}\begin{Bmatrix} \gamma_1 & 1 \\ 1 & 1/\gamma_2 \end{Bmatrix} - \frac{1}{2}(1 + \bar{k}_{z1}/\gamma_1)\begin{Bmatrix} 0 & 1 \\ 1 & 0 \end{Bmatrix}\right] \tag{24}$$

Note that the signs of the off-diagonal terms need to be reversed for the upper half space. Similarly, the stiffness matrices for a VTI layer and a half-space subjected to SH wave are derived and given in the form:

$$\mathbf{K} = kG_t\begin{Bmatrix} \mathbf{K}_{11} & \mathbf{K}_{12} \\ \mathbf{K}_{21} & \mathbf{K}_{22} \end{Bmatrix} = kG_t\frac{\bar{k}_{z3}}{S_3}\begin{Bmatrix} C_3 & -1 \\ -1 & C_3 \end{Bmatrix} \tag{25a}$$

$$\mathbf{K}_{half} = kG_t\bar{k}_{z3} \tag{25b}$$

The following parameters are defined for the VTI stiffness matrices presented above.

$$C_1 = \cosh k\bar{k}_{z1}h \tag{26a}$$

$$S_1 = \sinh k\bar{k}_{z1}h, \tag{26b}$$

$$C_2 = \cosh k\bar{k}_{z2}h, \tag{26c}$$

$$S_2 = \sinh k\bar{k}_{z2}h \tag{26d}$$

$$C_3 = \cosh k\bar{k}_{z3}h, \tag{26e}$$

$$S_3 = \sinh k\bar{k}_{z3}h, \tag{26f}$$

$$D_t = 2(1 - C_1C_2) + \left(\frac{\gamma_1}{\gamma_2} + \frac{\gamma_2}{\gamma_1}\right)S_1S_2 \tag{26g}$$

$$\bar{k}_{z1} \text{ or } \bar{k}_{z2} = \sqrt{\frac{\alpha^2(a^2 - 1) + 2 - (1 + \alpha^{-2})\Omega_{st}^2}{\sqrt{}} \pm \sqrt{[\alpha^2(a^2 - 1) - (1 - \alpha^{-2})\Omega_{st}^2]^2 + 4(a^2 - 1)(\alpha^2 - 1)}}{2}}$$

(dimensionless vertical wavenumbers for $P{-}SV$ wave)

$$\tag{26h,i}$$

$$\bar{k}_{z3} = \sqrt{b^2 - \Omega_{st}^2} \quad \text{(dimensionless vertical wavenumber for SH wave)} \tag{26j}$$

$$\gamma_1 = \frac{\alpha^2a^2 - \bar{k}_{z1}^2 - \Omega_{st}^2}{(\alpha^2 - 1)\bar{k}_{z1}}, \quad \gamma_2 = \frac{\alpha^2a^2 - \bar{k}_{z2}^2 - \Omega_{st}^2}{(\alpha^2 - 1)\bar{k}_{z2}},$$

(W/U ratio for $P{-}SV$ wave)

$$\tag{26k,l}$$

$$\Omega_{pt} = \frac{\omega}{kC_{pt}} = \frac{\Omega_{st}}{\alpha}, \Omega_{st} = \frac{\omega}{kC_{st}}, \quad \text{(dimensionless frequencies)}$$

$$\tag{26m,n}$$

The same topic was studied in [2], but only for the P-SV wave case, whereas the current study includes the SH wave case as well. In addition, the format and presentation of the matrices in the current study are more structured and compact than those in [2]. Therefore, they are more straightforward to be implemented in numerical codes based on

the stiffness matrix approach as in [1]. Note that by setting $a = 1$ and $b = 1$ in the VIT stiffness matrices, one can recover the stiffness matrices for the isotropic medium. Finally, it is important to note that all the parameters used in Eqs. (23–24) are functions of α, a and Ω_{st}, but independent of b. This implies that the horizontal wave speed (C_s) is not contributing to the P-SV mode, which is also a finding of the present study.

3. Impedances of foundations on anisotropic soil

Both as a verification of the developed solution, and investigation of the effect of soil anisotropy on the stiffness and damping of rigid foundations, the complex impedances of a rigid square footing resting on a homogeneous soil layer over a half-space are calculated and compared with those for isotropic soil [11]. The technique used here to calculate the impedance is based on the one proposed in [12]. According to this technique, the contact surface between the ground and foundation is discretized into a regular grid of rectangular elements. By applying uniformly distributed unit loads on each element in the three directions and calculating the displacements at all element centres (nodes), one can derive the flexibility matrix of the ground-foundation interface which is a relationship between the forces and the corresponding nodal displacements. By imposing the rigid-body motion of the footing for the desired mode of response (horizontal, rocking and vertical) and summing the contributions from the element loads one can compute the forces and moments on the foundation which define the elements of the foundation impedance matrix.

The following parameters are used for the top soil layer: C_{st1} = 150 m/s, ρ_1 = 1770 kg/m^3, damping ratio, ξ_1 = 0.05. The corresponding parameters for the half-space are C_{st2} = 250 m/s, ρ_2 = 2000 kg/m^3 and ξ_2 = 0.03. The pressure wave velocities in the whole soil system (C_{pt1}, C_{pt2}) are taken as 1500 m/s. The dimensions of the foundation (2d) and layer thickness (h) are both 4 m. See Fig. 2 for schematic description of the model of interest. An 8×8 grid is used to discretize the foundation and the impedances are calculated for frequencies (ω) ranging from 0.0 (static) to 300.0 rad/s. This range corresponds to the non-dimensional frequency $\omega d/C_{st1}$ between 0.0 and 4.0. To present the results, the horizontal and vertical impedance terms are normalized by $G_{t1}d$ and the rocking and torsional impedances were normalized by $G_{t1}d^3$, where G_{t1} = $\rho_1C_{st1}^2$ is the shear modulus of the top soil layer.

Fig. 3(a-d) display the real and imaginary parts of the calculated normalized impedances for the horizontal, vertical, rocking and torsional responses for the ground/foundation system considered. Also plotted in these figures are the results reported in [11]. Good agreement is observed between the two solutions. The minor differences are due to the discretization of the foundation. A finer mesh will bring the two solutions closer.

Fig. 4(a-d) displays the normalized impedances of a square foundation on a homogeneous half space with properties as the top soil layer in the preceding analysis. The figures plot the results for several cases as follows: 1) Isotropic soil (denoted "Isotropic"), 2) Anisotropic soil 1 with same parameters as in "Isotropic" but with anisotropy factors $a = b = 1.2$ (denoted as "VTI-1"), 3) Anisotropic soil 2 with same parameters as in "Isotropic" but with anisotropy factors $a = b = 1.5$ (denoted as "VTI-2"), and 4) Anisotropic soil similar to "VTI-2" with 100 m water over half-space (denoted "VTI-2 + 100 m water"). The figures show the general trends known from the classical solutions for isotropic soil media; that is, the real part decreasing with frequency, indicating the effect of added soil mass, and the imaginary part increasing almost linearly with frequency, indicating a viscous type radiation damping. The effect of anisotropy is reflected by the increase in the initial stiffness and damping, and the effect of water is seen as an increased added mass in the vertical and rocking responses. The latter observation and trend are consistent with those reported in other literature [6].
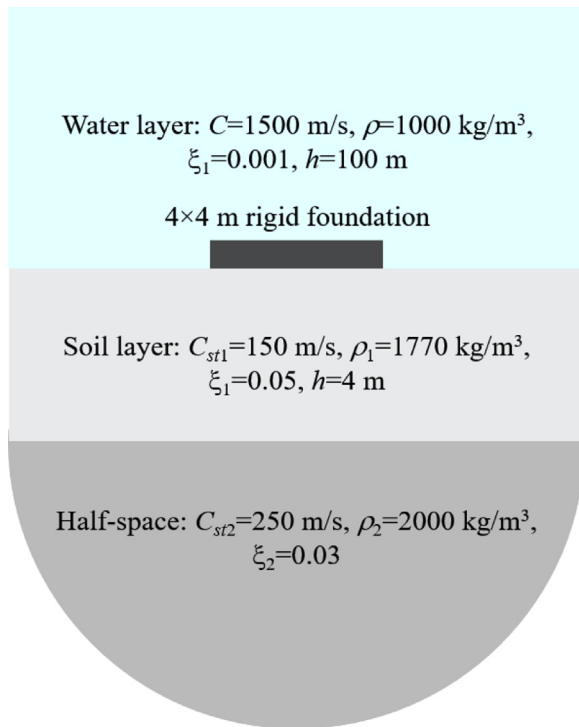
Fig. 2. Schematic model description of foundation on layered soil half-space under 100 m water.

4. Rayleigh and Love waves in anisotropic half space

The Rayleigh surface wave is a non-dispersive P-SV mode that propagates laterally without any significant attenuation near the top surface of a homogeneous half-space. For an isotropic homogenous half-space, the velocity of the Rayleigh wave ($C_{Rayleigh}$) is well known and can be approximated as $C_{Rayleigh} \sim (0.197\nu + 0.874)C_s$ where ν and C_s

are the Poisson's ratio and S-wave velocity of the soil. In a VTI medium, the situation is more complicated, because the velocities in the horizontal (C_s and C_p) and vertical (C_{st} and C_{pt}) directions are different. Therefore, the velocity of the Rayleigh wave depends not only on the Poisson's ratio and S-wave velocity, but also on the ratio $a = C_{pt}/C_p$. The so-called characteristic equation for the Rayleigh surface wave can be obtained by finding Ω_{st} that makes the determinant of $\mathbf{K}_{half}$ zero. By applying Eq. (24) to this condition, we can derive the following simple characteristic equation for the Rayleigh surface wave of a VTI homogeneous medium:

$$\frac{1}{(\gamma_2 - \gamma_1)} \left[\frac{(\overline{k}_{z1} + \gamma_1)^2}{\gamma_1} - \frac{(\overline{k}_{z2} + \gamma_2)^2}{\gamma_2} \right] = 0 \qquad (27)$$

The value of Ω_{st} that satisfies this characteristic equation is equivalent to the ratio of $C_{Rayleigh}/C_{st}$. Note that Ω_{st} is defined as $\omega/k/C_{st}$, and ω/k becomes $C_{Rayleigh}$, when Ω_{st} satisfies Eq. (27). To illustrate the effect of VTI on Rayleigh waves, we calculate the Rayleigh surface phase velocity for a set of different α's and plot vs. a in Fig. 5(a). It is observed that as the two ratios of α and a increase, $C_{Rayleigh}$ converges to C_{st}. This implies that for such cases, the Rayleigh surface wave may propagate at almost the same speed as the vertical S-wave velocity (C_{st}). Nevertheless, it is still true that the Rayleigh surface wave in a VTI medium is non-dispersive (i.e. independent of frequency). Fig. 5(b) shows an example of synthetic seismogram of radial acceleration calculated at 5 km offset on the surface of a VTI homogeneous medium subjected to a horizontal (x-direction) impulsive point load. The model parameters of the VTI medium are $C_{st} = 556$ m/s, $a = 1.225$, and $\alpha = 2$. The solid curve is the seismogram for the VTI medium case and the dashed curve is for the corresponding isotropic medioum (i.e. $a = 1$). The corresponding Rayleigh phase velocity is also shown by the dashed curve in Fig. 5(a). The wave arrival for the vertical S-wave velocity (C_{st}) is around 9 s (≈ 5 km/556 m/s), right after which the Rayleigh wave arrives with large magnitude as shown in Fig. 5(b). Finally, Fig. 5(c,d) illustrate the normalized mode shape variations along the normalized depth for a given α of 2 and various a's. It is observed that as the parameter a increases, the penetration depth for the horizontal motion
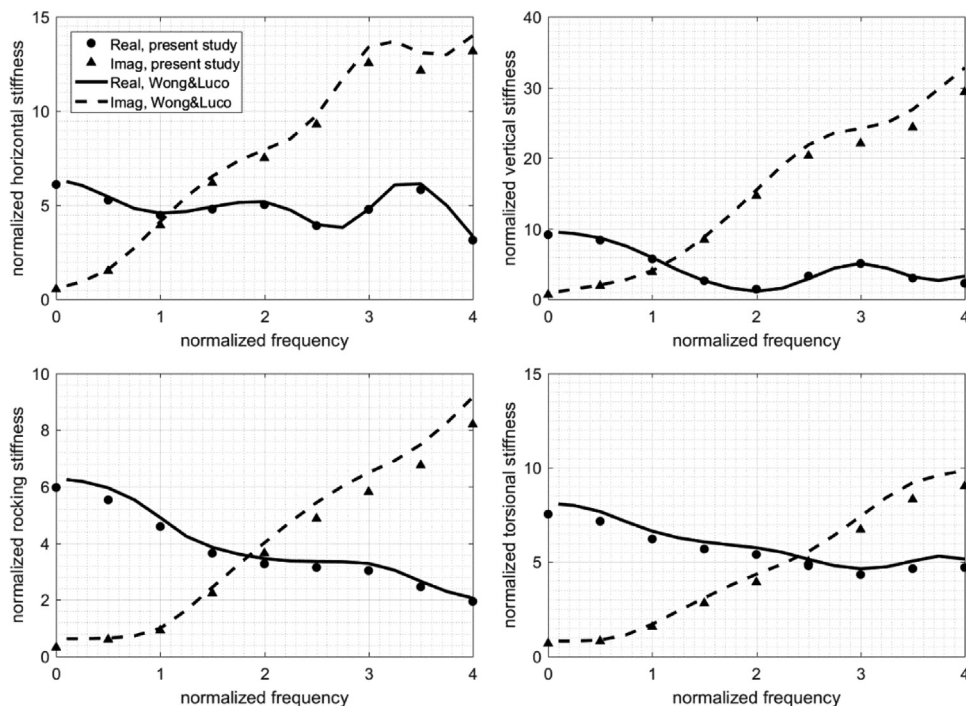

Fig. 3. Impedances of rigid square block on two-layer half-space: Present study (symbols) versus [11] (solid and dashed lines) – Real indicates Real part and Imag. indicates Imaginary part.
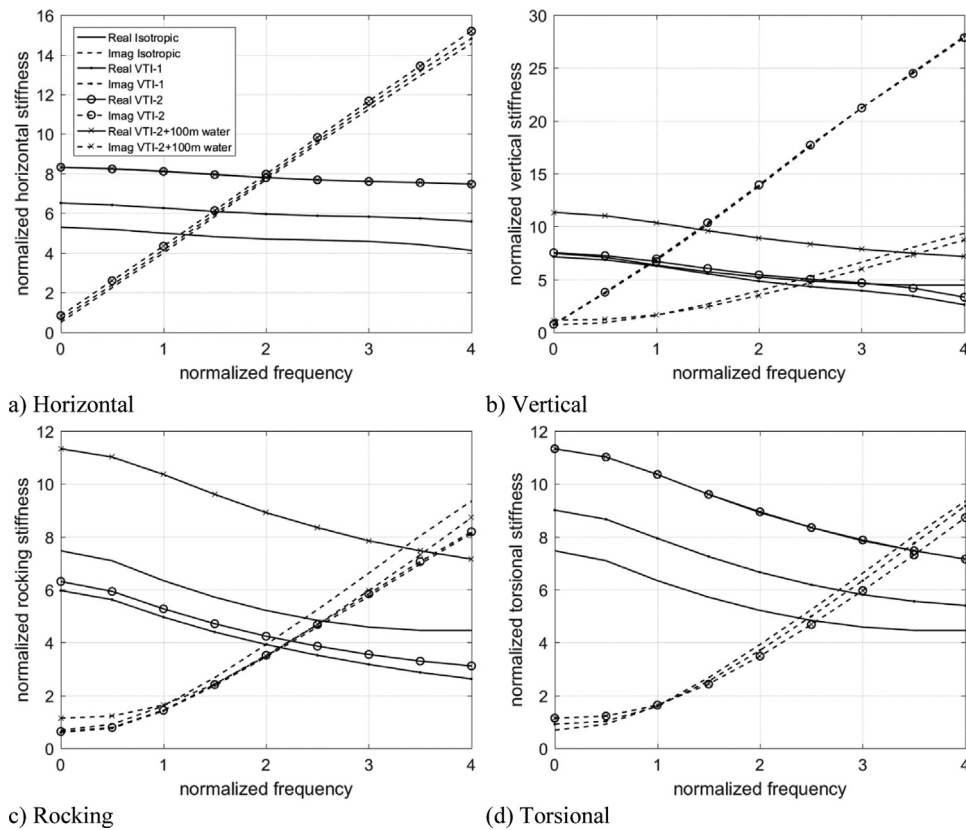
Fig. 4. Impedances of rigid square block on isotropic and anisotropic half spaces and effect of water: Real and Imag indicate, real and imaginary parts, respectively.

decreases significantly, while that of the vertical motion becomes larger (compared to about two wavelengths for the isotropic medium). Such information is important, for example in the context of the spectral analysis of surface waves (SASW) where the estimated wavelength is related to the soil depth profile.

For a homogeneous soil layer over a half-space, there exist a group of guided SH modes (Love waves) that propagate laterally only within the upper layer. The Love wave is not only dispersive, but also has multiple modes (or poles) for a given frequency. The condition for the Love wave to exist is that the wave speed of the upper layer be smaller than that of the lower half-space. A VTI medium has two different wave velocities along the horizontal (C_s) and vertical (C_{st}) directions. Therefore, the Love wave's behavior in a VTI medium is more complicated than that in an isotropic medium. We illustrate this with a set of numerical examples and by tuning the velocities of the layers and their contrasts. We fix the densities of the layer and half-space and the layer thickness to $\rho_1 = 1$ g/cm^3, $\rho_2 = 2$ g/cm^3 and $h = 1$ km, and consider four different combinations of ($C_{s1}, C_{st1}, C_{s2}, C_{st2}$) as (1,1,3,3), (2,2,3,3), (1,2,3,3) and (2,1,3,3) km/s. The results are presented in Fig. 6 that plot the phase velocity of the Love wave (C_{ph}) versus frequency. As expected, the Love wave in the VTI medium shows dispersive and multiple modes. It should be noticed that the range of the phase velocity is not simply between the slowest and fastest velocities, which is the case for an isotropic medium. For example, the upper layer's horizontal velocity (C_{s1}) governs the lower limit of phase velocity of the Love wave. On the other hand, the upper layer's vertical velocity (C_{st1}) together with the upper layer's horizontal velocity (C_{s1}) has influence on the number of modes for a given frequency range. This observation is important in the searching technique for propagation modes, for example in multichannel analysis of surface waves (MASW).

5. Vertical point load applied to layered half-spaces

To investigate the effect of anisotropy on wave propagation, we set

up three different synthetic models. To this end, we consider a three-layer model with parameters listed in Table 1, and we vary the values of *a* and *b* according to Table 2. In Model 1, all the three layers are isotropic. In Model 2, the bottom two layers are anisotropic, while the top layer is isotropic. Finally, in Model 3, all the three layers are anisotropic.

To generate waves, we apply a vertical impulse point load of Hanning shape with the loading period of 0.02 s (e.g. [9]). We compare the seismograms calculated at the top surface in terms of vertical particle velocity. Fig. 7 shows the results in the offset-time space, and the gray scale indicates the relative intensity of the vertical particle velocity. The same scale is applied to all the three results and is suppressed in order to show more clearly the reflected/refracted waves (which otherwise could be difficult to see due to the large amplitudes of the Rayleigh wave). The results of Models 1 and 2 in Fig. 7(a) and (b) look similar, because the top layer is the same for the two models and the point load and receivers are all located on the top surface. However, the reflected and refracted waves arriving at far offset (> 5 km) show different behaviors between Models 1 and 2. On the other hand, the Rayleigh wave propagations of the two models are almost identical, which can be explained by the fact that the Rayleigh wave propagates only along the surface and the thickness of the top layer is large enough so that the surface wave doesn't feel the second layer. The wave pattern in Fig. 7(c) is quite different from those in Fig. 7(a) and (b). The P and S direct waves in Fig. 7(c) arrive much earlier than those in Fig. 7(a) and (b). The Rayleigh surface wave also arrives earlier than in the isotropic top layer case, and its magnitude is smaller than the isotropic case, which is also observed in Fig. 5(b). In general, the wave pattern in the fully anisotropic medium (Model 3) is not only different, but also more complex than those of Models 1 and 2 at both near offset and far offset. For example, when the first P-wave reflection from the top of the second layer arrives the top surface ($t = 1.66$ s and at almost zero offset) and propagates further, another new wave component develops even at very short offset. This wave propagates slowly but its magnitude
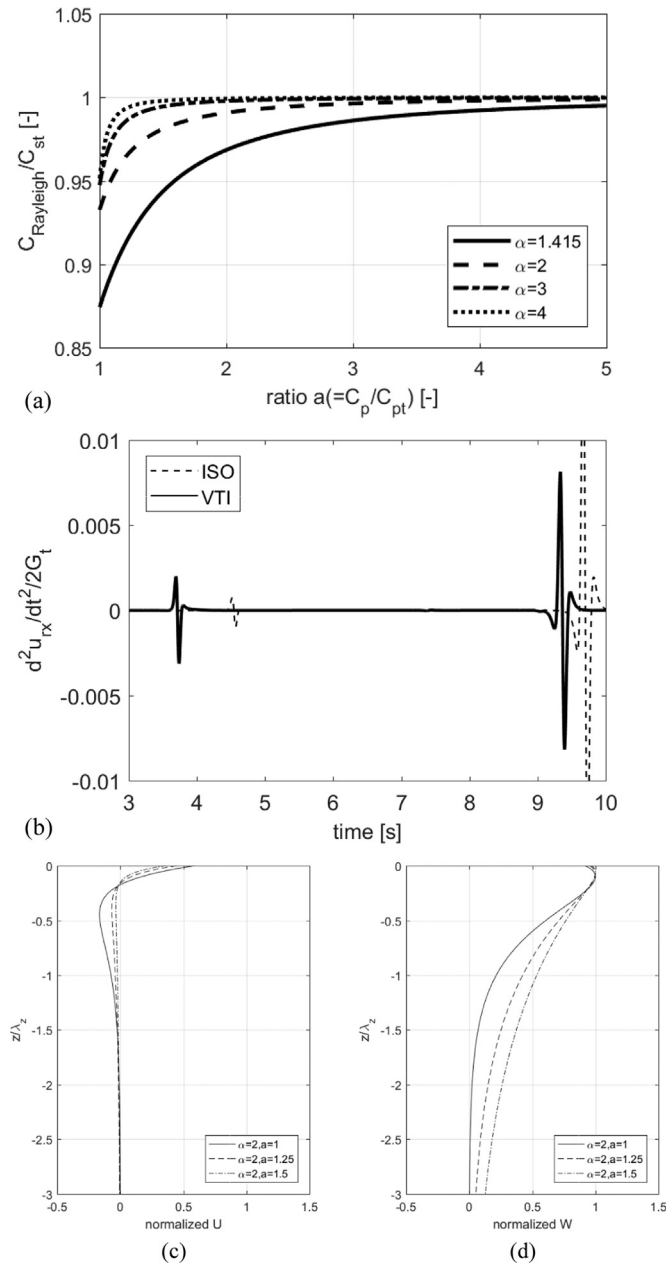
Fig. 5. Rayleigh surface wave in a VTI half-space: (a) Phase velocity of Rayleigh surface wave ($C_{Rayleigh}$) for a VTI homogeneous half-space as function of $a = C_p/C_{pt}$ for different $\alpha = C_{pt}/C_{st}$; (b) synthetic seismogram of radial acceleration calculated at offset $x = 5$ km on top surface due to a horizontal (x-direction) point load with $C_{st} = 556$ m/s, $a = 1.225$, and $\alpha = 2$; (c, d) normalized horizontal (U) and vertical (W) mode shapes with depth (z/λ_z) for $\alpha = 2$ and $a = 1$, 1.25, 1.5.

is increasing significantly near 5 km offset and later decreases again. This example demonstrates the importance of applying the right material model, that is, isotropic or anisotropic.

6. Discontinuity seismic sources

In this section, we explore the possibility of simulating a group of seismic sources such as explosive blast, fault rupture, and marine air-gun, which require additional developments in order to fit into the layer

stiffness matrix approach. Such sources have successfully been dealt with by, among others [13–15] using methods other than the stiffness matrix formulation. Normally, the layer stiffness matrix approach applies the force discontinuity by including the externally applied nodal load in the loading vector on the right hand side of the system of equations. However, the same approach cannot be used when simulating blasts, fault rupture and marine air-gun sources that are represented by displacement discontinuity.

It should be noted that the marine air-gun source, which is a standard source in offshore exploration, can readily be modelled by using the acoustic layer stiffness matrix approach that is formulated by means of the velocity potential and pressure (Eqs. 9 and 11) without applying the displacement discontinuity. This is because the term for the volume change on the right hand side of Eqs. (9 and 11) represents exactly the marine air-gun source. Herein, however, we consider the layer stiffness matrix approach that is formulated through displacements (Eq. (12) and 23–25).

A typical equation of motion of the layer stiffness matrix approach formulated in terms of displacement for an N-layer system over a half-space is expressed as

$$
\begin{Bmatrix}
\mathbf{K}_{11}^1 & \mathbf{K}_{12}^1 \\
\mathbf{K}_{21}^1 & \ddots \\
& & \mathbf{K}_{22}^{i-2}+\mathbf{K}_{11}^{i-1} & \mathbf{K}_{12}^{i-1} \\
& & \mathbf{K}_{21}^{i-1} & \mathbf{K}_{22}^{i-1}+\mathbf{K}_{11}^{i} & \mathbf{K}_{12}^{i} \\
& & & \mathbf{K}_{21}^{i} & \mathbf{K}_{22}^{i}+\mathbf{K}_{11}^{i+1} \\
& & & & & \ddots & \mathbf{K}_{12}^N \\
& & & & & \mathbf{K}_{21}^N & \mathbf{K}_{22}^N+\mathbf{K}_{half}
\end{Bmatrix}
$$

$$
\begin{Bmatrix}
\mathbf{u}_1 \\ \vdots \\ \mathbf{u}_{i-1} \\ \mathbf{u}_i \\ \mathbf{u}_{i+1} \\ \vdots \\ \mathbf{u}_N
\end{Bmatrix}
=
\begin{Bmatrix}
\mathbf{p}_1 \\ \vdots \\ \mathbf{p}_{i-1} \\ \mathbf{p}_i \\ \mathbf{p}_{i+1} \\ \vdots \\ \mathbf{p}_N
\end{Bmatrix}
\tag{28}
$$

in which $\mathbf{K}_{11}^i$, $\mathbf{K}_{12}^i$, $\mathbf{K}_{21}^i$ and $\mathbf{K}_{22}^i$ are the 3×3 elements in the stiffness matrix for layer i (Eq. (23–25)) and both of the P-SV and SH modes are included. In addition, $\mathbf{u}_i$ and $\mathbf{p}_i$ are the displacement and force vectors at interface i indicating top interface of layer i.

When a discontinuous seismic source such as blast, fault rupture, and marine air-gun is applied at an interface, a displacement discontinuity arises. The magnitude of the discontinuity can be represented by $\delta\mathbf{u} = [\ \delta U,\ \delta V,\ \delta W]^T$ defined in the wavenumber domain. Then, we can write the displacement discontinuity as

$$
\mathbf{u}_i^{upper} - \mathbf{u}_i^{lower} = \delta\mathbf{u}
\tag{29}
$$

Next, we can disassemble the whole system of equations into the upper and lower parts, as given by:

$$
\begin{Bmatrix}
\ddots \\
\mathbf{K}_{22}^{i-2}+\mathbf{K}_{11}^{i-1} & \mathbf{K}_{12}^{i-1} \\
\mathbf{K}_{21}^{i-1} & \mathbf{K}_{22}^{i-1}
\end{Bmatrix}
\begin{Bmatrix}
\vdots \\ \mathbf{u}_{i-1} \\ \mathbf{u}_i^{upper}
\end{Bmatrix}
=
\begin{Bmatrix}
\vdots \\ \mathbf{p}_{i-1} \\ \mathbf{p}_i^{upper}
\end{Bmatrix}
\tag{30a}
$$

$$
\begin{Bmatrix}
\mathbf{K}_{11}^{i} & \mathbf{K}_{12}^{i} \\
\mathbf{K}_{21}^{i} & \mathbf{K}_{22}^{i}+\mathbf{K}_{11}^{i+1} \\
& & \ddots
\end{Bmatrix}
\begin{Bmatrix}
\mathbf{u}_i^{lower} \\ \mathbf{u}_{i+1} \\ \vdots
\end{Bmatrix}
=
\begin{Bmatrix}
\mathbf{p}_i^{lower} \\ \mathbf{p}_{i+1} \\ \vdots
\end{Bmatrix}
\tag{30b}
$$

In the case of no displacement discontinuity, the following relationships hold.

$$
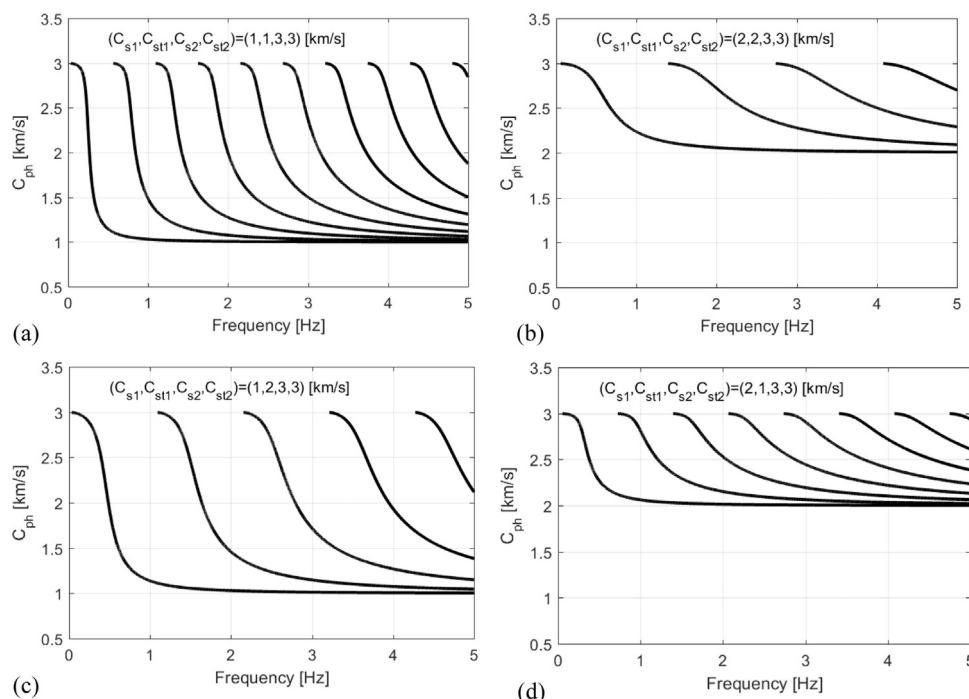\mathbf{u}_i^{upper} = \mathbf{u}_i^{lower} = \mathbf{u}_i
\tag{31a}
$$

Fig. 6. Phase velocity (C_{ph}) of Love waves versus frequency for a VTI layer over an isotropic half-space: (a)-(d) show four different S-wave velocity profiles.

Table 1
Parameters of three layered model.

Layer	Thickness [m]	Density [kg/m³]	C_{st} [m/s]	C_{pt} (m/s)
1	500	2400	200	600
2	500	2400	400	800
3	Half space	2400	1200	2000

Table 2
Anisotropy parameters a and b for three different models.

Layer	Model 1 (fully isotropic)		Model 2 (partially VTI)		Model 3 (fully VTI)	
	a	b	a	b	a	b
1	1.0	1.0	1.0	1.0	1.5	1.5
2	1.0	1.0	1.5	1.5	1.5	1.5
3	1.0	1.0	1.5	1.5	1.5	1.5

$$\mathbf{p}_i^{upper} + \mathbf{p}_i^{lower} = \mathbf{p}_i \tag{31b}$$

However, when the displacement discontinuity exists as shown in Eq. (29), the first of the two relationships above no longer holds. Instead, the displacement discontinuity shown above should be applied for example to the upper part of the system of equations as

$$\begin{Bmatrix} \ddots & & \\ & \mathbf{K}_{22}^{i-2} + \mathbf{K}_{11}^{i-1} & \mathbf{K}_{12}^{i-1} \\ & \mathbf{K}_{21}^{i-1} & \mathbf{K}_{22}^{i-1} \end{Bmatrix} \begin{Bmatrix} \vdots \\ \mathbf{u}_{i-1} \\ \mathbf{u}_i^{lower} + \delta\mathbf{u} \end{Bmatrix} = \begin{Bmatrix} \vdots \\ \mathbf{p}_{i-1} \\ \mathbf{p}_i^{upper} \end{Bmatrix} \tag{32}$$

For a known discontinuity $\delta\mathbf{u}$, we can rearrange the upper part of the equations to derive the following equation:

$$\begin{Bmatrix} \ddots & & \\ & \mathbf{K}_{22}^{i-2} + \mathbf{K}_{11}^{i-1} & \mathbf{K}_{12}^{i-1} \\ & \mathbf{K}_{21}^{i-1} & \mathbf{K}_{22}^{i-1} \end{Bmatrix} \begin{Bmatrix} \vdots \\ \mathbf{u}_{i-1} \\ \mathbf{u}_i^{lower} \end{Bmatrix} = \begin{Bmatrix} \vdots \\ \mathbf{p}_{i-1} \\ \mathbf{p}_i^{upper} \end{Bmatrix} - \begin{Bmatrix} \vdots \\ \mathbf{K}_{12}^{i-1}\delta\mathbf{u} \\ \mathbf{K}_{22}^{i-1}\delta\mathbf{u} \end{Bmatrix} \tag{33}$$

By reassembling the systems of equations for the upper and lower parts, we can obtain the following modified equation for the whole system:

$$\begin{Bmatrix} \mathbf{K}_{11}^1 & \mathbf{K}_{12}^1 & & & & & & \\ \mathbf{K}_{21}^1 & \ddots & & & & & & \\ & & \mathbf{K}_{22}^{i-2} + \mathbf{K}_{11}^{i-1} & \mathbf{K}_{12}^{i-1} & & & & \\ & & \mathbf{K}_{21}^{i-1} & \mathbf{K}_{22}^{i-1} + \mathbf{K}_{11}^{i} & \mathbf{K}_{12}^{i} & & \\ & & & \mathbf{K}_{21}^{i} & \mathbf{K}_{22}^{i} + \mathbf{K}_{11}^{i+1} & & \\ & & & & & \ddots & \mathbf{K}_{12}^{N} \\ & & & & & \mathbf{K}_{21}^{N} & \mathbf{K}_{22}^{N} + \mathbf{K}_{half} \end{Bmatrix}$$

$$\begin{Bmatrix} \mathbf{u}_1 \\ \vdots \\ \mathbf{u}_{i-1} \\ \mathbf{u}_i^{lower} \\ \mathbf{u}_{i+1} \\ \vdots \\ \mathbf{u}_N \end{Bmatrix} = \begin{Bmatrix} \mathbf{0} \\ \vdots \\ -\mathbf{K}_{12}^{i-1}\delta\mathbf{u} \\ -\mathbf{K}_{22}^{i-1}\delta\mathbf{u} \\ \mathbf{0} \\ \vdots \\ \mathbf{0} \end{Bmatrix} \tag{34}$$

in which we assume that there is no external applied force (i.e. $\mathbf{p}_i = 0$), except the displacement continuity resulting from marine air-gun, fault rupture, or blast. We can now solve the whole system of equations and obtain the response by following the same procedure as in [1].

6.1. Acoustic source or air-gun

We solve a simple case of an acoustic source of marine air-gun type that is applied at the interface ($z = 0$) between two isotropic homogeneous fluid half-spaces whose properties are identical. We apply the stiffness matrix in Eq. (12), instead of Eqs. (9 and 11), to demonstrate how the seismic source modeling approach discussed in this section can be handled. The relevant stiffness matrix for a homogeneous half-space can be expressed as

$$\frac{\rho\omega^2}{\beta} u_z^{upper} = \tau^{upper} \tag{35a}$$

$$\frac{\rho\omega^2}{\beta} u_z^{lower} = \tau^{lower} \tag{35b}$$

which can be derived by applying $h \to \infty$ in Eq. (12) and using the two
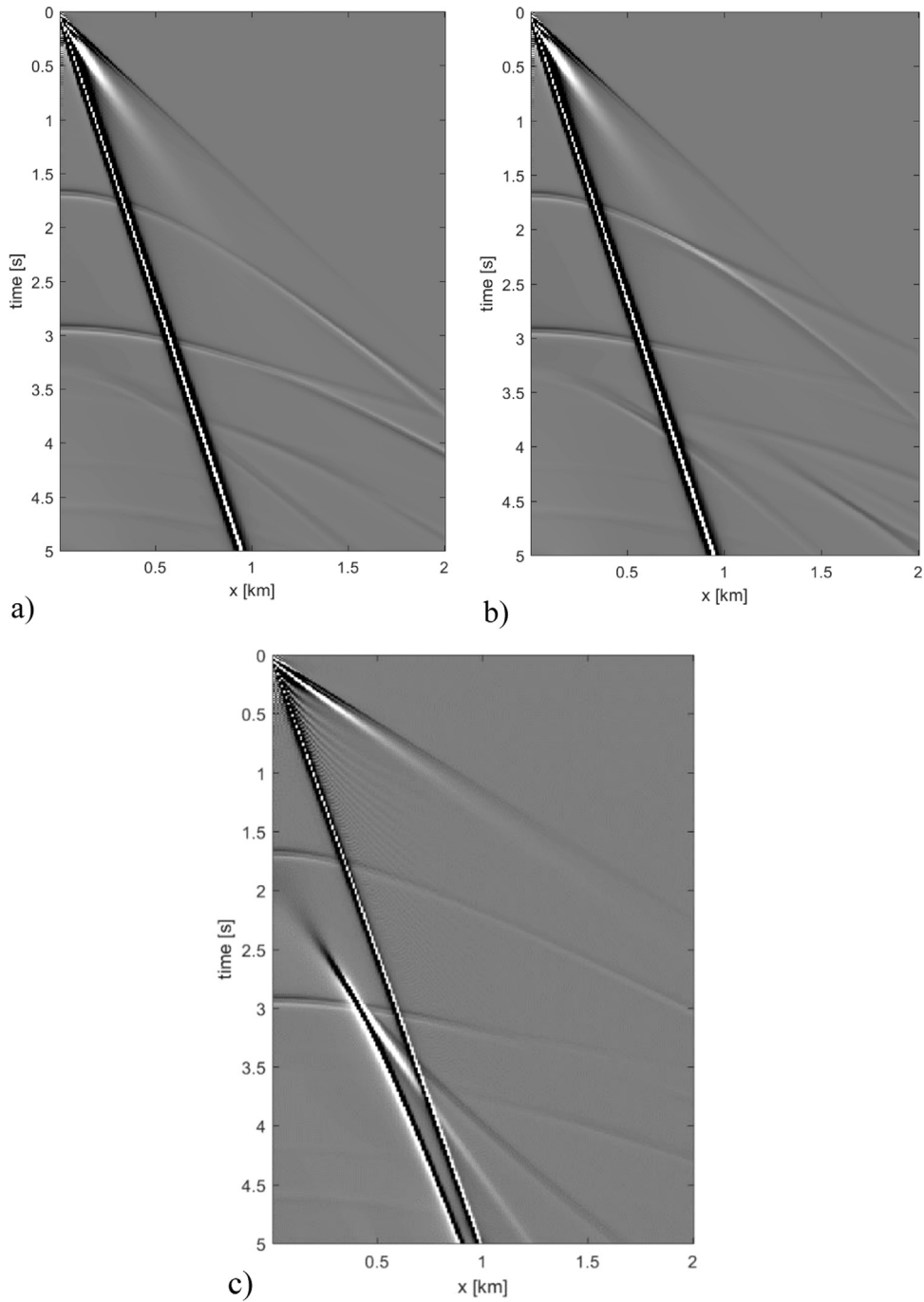
Fig. 7. Seismograms of vertical particle velocity calculated on top surface of three layered half-spaces excited by a vertical impulse load applied at the top surface: (a) Model 1: fully isotropic layers; (b) Model 2: partially VTI layers, and (c) Model 3: fully VTI layers. Details of models are given in Tables 1 and 2.

diagonal terms: one representing the stiffness matrix for the lower half-space and the other representing the upper half-space. It should be noted that in the current case, as well as the SH wave case, the two diagonal terms are identical, which is not the case with the P-SV wave case. When assembled together, the sum of the two diagonal terms represents the stiffness matrix for the full space. The displacement discontinuity can be expressed as

$$u_z^{upper} - u_z^{lower} = \frac{\bar{v}^*}{i\omega} \tag{36}$$

where $\bar{v}^*$ is the injected or increased volume rate (in velocity) by an air-gun seismic source. After assembling the two stiffness matrices by using the displacement discontinuity in Eq. (36), we obtain the following

equation:

$$\frac{\rho\omega^2}{\beta}\left(u_z^{lower} + \frac{\bar{v}^*}{i\omega}\right) + \frac{\rho\omega^2}{\beta}u_z^{lower} = 0 \tag{37}$$

The solution of this equation leads to the vertical displacement of the lower half-space at the interface between the two half-spaces (i.e. $z = 0$), given by:

$$u_z^{lower} = -\frac{\bar{v}^*}{2i\omega} \tag{38}$$

On the other hand, the same problem can be solved by applying either of Eqs. (9) and (11). For example, utilizing Eq. (9) and again applying $h \rightarrow \infty$, we can obtain the velocity potential at the interface and
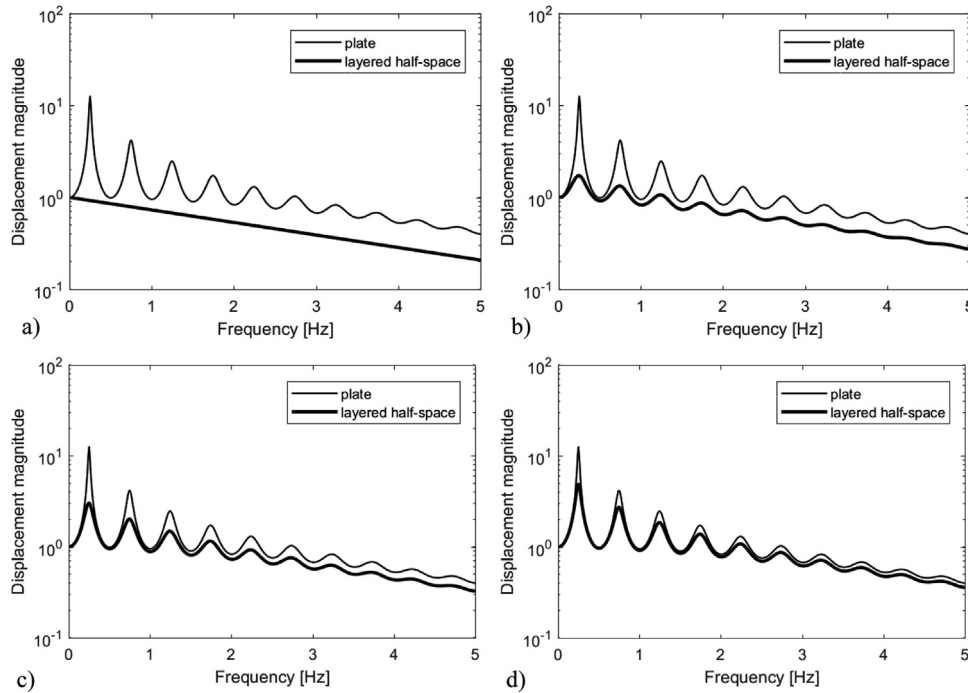
Fig. 8. Displacement magnitude on top surface of a layer with $C_{s1} = 1$ km/s over a half-space (thick lines) subjected to displacement discontinuity at interface compared with a plate (thin lines) for increasing velocity of half-space: (a) $C_{s2} = 1$ km/s; (b) $C_{s2} = 2$ km/s; (c) $C_{s2} = 4$ km/s; (d) $C_{s2} = 8$ km/s.

then calculate the vertical displacement for the lower half-space through the following procedure.

$$u_z^{lower} = \frac{1}{i\omega} \frac{\partial \phi(z)}{\partial z}\bigg|_{z=0} = -\frac{\bar{v}^*}{2i\omega} \tag{39}$$

where $\phi(z) = \frac{\bar{v}^*}{2\beta} e^{-\beta z}$ and $\mathrm{Im}\,\beta \leq 0$. Note that the results of the two methods are identical.

6.2. Slip motion at large-stiffness-contrast interface

In this section, we consider another example in which a homogeneous layer over a half-space is subjected to a displacement discontinuity at the interface. We explore an interesting feature of the model by increasing the stiffness ratio between the half-space and the layer ($G_{half\text{-}space}/G_{layer}$). Note that $G_{half\text{-}space}$ and G_{layer} herein are the shear stiffness related to the vertical wave propagation (i.e. G_t). The equation for the system can be written as

$$\begin{Bmatrix} \mathbf{K}_{11}^1 & \mathbf{K}_{12}^1 \\ \mathbf{K}_{21}^1 & \mathbf{K}_{22}^1 \end{Bmatrix} \begin{Bmatrix} \widetilde{\mathbf{u}}_1 \\ \widetilde{\mathbf{u}}_2^{upper} \end{Bmatrix} = \begin{Bmatrix} \mathbf{0} \\ \widetilde{\mathbf{p}}_2^{upper} \end{Bmatrix} \quad \text{(upper homogeneous layer)} \tag{40a}$$

$$\mathbf{K}_{half}^2 \widetilde{\mathbf{u}}_2^{lower} = \widetilde{\mathbf{p}}_2^{lower} \quad \text{(lower homogeneous half–space)} \tag{40b}$$

$$\widetilde{\mathbf{u}}_2^{upper} - \widetilde{\mathbf{u}}_2^{lower} = \delta\mathbf{u} \quad \text{(displacement discontinuity)} \tag{40c}$$

$$\widetilde{\mathbf{p}}_2^{upper} + \widetilde{\mathbf{p}}_2^{lower} = \mathbf{0} \quad \text{(force continuity/equilibrium)} \tag{40d}$$

Then, the equation of motion of the half-space can be expressed in terms of $\widetilde{\mathbf{u}}_2^{upper}$ (i.e. nodal displacement vector at the bottom of the upper layer) as

$$\mathbf{K}_{half}^2 \widetilde{\mathbf{u}}_2^{upper} = \widetilde{\mathbf{p}}_2^{lower} + \mathbf{K}_{half}^2 \delta\mathbf{u} \tag{41}$$

By assembling the matrix equations for the whole system, we obtain the following equation:

$$\begin{Bmatrix} \mathbf{K}_{11}^1 & \mathbf{K}_{12}^1 \\ \mathbf{K}_{21}^1 & \mathbf{K}_{22}^1 + \mathbf{K}_{half}^2 \end{Bmatrix} \begin{Bmatrix} \widetilde{\mathbf{u}}_1 \\ \widetilde{\mathbf{u}}_2^{upper} \end{Bmatrix} = \begin{Bmatrix} \mathbf{0} \\ \mathbf{K}_{half}^2 \delta\mathbf{u} \end{Bmatrix} \tag{42}$$

Multiplication of both sides by $[\mathbf{K}_{half}^2]^{-1}$ then leads to:

$$\begin{Bmatrix} [\mathbf{K}_{half}^2]^{-1}\mathbf{K}_{11}^1 & [\mathbf{K}_{half}^2]^{-1}\mathbf{K}_{12}^1 \\ [\mathbf{K}_{half}^2]^{-1}\mathbf{K}_{21}^1 & [[\mathbf{K}_{half}^2]^{-1}\mathbf{K}_{22}^1 + \mathbf{I}] \end{Bmatrix} \begin{Bmatrix} \widetilde{\mathbf{u}}_1 \\ \widetilde{\mathbf{u}}_2^{upper} \end{Bmatrix} = \begin{Bmatrix} \mathbf{0} \\ \delta\mathbf{u} \end{Bmatrix} \tag{43}$$

As the ratio of $G_{half\text{-}space}/G_{layer}$ increases, the magnitude of $\mathbf{K}_{half}^2$ will dominate compared to $\mathbf{K}^1$. Therefore, the left hand side of the equation above can be simplified as

$$\lim_{\frac{G_{half-space}}{G_{layer}} \to \infty} \begin{Bmatrix} [\mathbf{K}_{half}^2]^{-1}\mathbf{K}_{11}^1 & [\mathbf{K}_{half}^2]^{-1}\mathbf{K}_{12}^1 \\ [\mathbf{K}_{half}^2]^{-1}\mathbf{K}_{21}^1 & [[\mathbf{K}_{half}^2]^{-1}\mathbf{K}_{22}^1 + \mathbf{I}] \end{Bmatrix} \begin{Bmatrix} \widetilde{\mathbf{u}}_1 \\ \widetilde{\mathbf{u}}_2^{upper} \end{Bmatrix}$$
$$\to \begin{Bmatrix} \mathbf{0} & \mathbf{0} \\ \mathbf{0} & [\mathbf{0} + \mathbf{I}] \end{Bmatrix} \begin{Bmatrix} \widetilde{\mathbf{u}}_1 \\ \widetilde{\mathbf{u}}_2^{upper} \end{Bmatrix} \tag{44}$$

which results in the solution $\widetilde{\mathbf{u}}_2^{upper} \approx \delta\mathbf{u}$. Once $\widetilde{\mathbf{u}}_2^{upper}$ is known, then the system of equations can be written as

$$\begin{Bmatrix} \mathbf{K}_{11}^1 & \mathbf{K}_{12}^1 \\ \mathbf{K}_{21}^1 & \mathbf{K}_{22}^1 \end{Bmatrix} \begin{Bmatrix} \widetilde{\mathbf{u}}_1 \\ \delta\mathbf{u} \end{Bmatrix} = \begin{Bmatrix} \mathbf{0} \\ \widetilde{\mathbf{p}}_2 \end{Bmatrix} \tag{45}$$

This equation is nothing but the equation for a homogeneous layer or plate subjected to a given displacement at the bottom boundary. Therefore, it is shown that as the ratio of $G_{half\text{-}space}/G_{layer}$ increases, a homogeneous layer over a half-space may behave almost like a homogeneous plate, as the displacement discontinuity is applied at the interface.

We elaborate this example by presenting a set of numerical problems. The displacement discontinuity at the interface is specified only along the θ direction, i.e. SH (or pure torsional) wave case. In addition, we assume the radial wavenumber equal to zero i.e. $k = 0$. That is, only the vertical propagation is of interest. For more simplicity, we consider an isotropic medium. The density, S-wave velocity and thickness of the upper layer are taken as $\rho = 1$ g/cm^3, $C_{s1} = 1$ km/s and $h = 1$ km, respectively. We vary the S-wave velocity of the half-space (C_{s2}) in order to study its effect on the response of the layer. The density of the half-space is also assumed 1 g/cm^3. Fig. 8 shows the magnitude of the θ-direction displacement at the top of the layer (thick curves) as function

of frequency for different C_{s2} of 1, 2, 4 and 8 km/s corresponding to stiffness contrasts between the half-space and the upper layer ($G_{half-space}/G_{layer}$) equal to 1, 4, 16 and 64, respectively. The thin curve in Fig. 8 represents the responses of the plate case. It can be seen that the two curves converge which means that as $G_{half-space}/G_{layer}$ increases, the layer over the half-space behaves like a plate.

7. Derivation of PML parameters

The perfectly matched layer (PML) technique is a powerful method for removing or minimizing artificial reflections from the boundaries of computational domains. Such reflections are inevitable in numerical methods such as finite difference and finite element. The basic idea of PML is to stretch the spatial coordinate into a complex-valued large-scale one, through which the incident waves into the PML domain die out and no significant artificial reflection occurs at the computational boundary. Various PML applications have been reported in the literature. The real-value stretching approach that was implemented in SASSI [16] is probably the first solution. [17] developed an approach by means of field splitting in finite difference simulation of electromagnetics. Since then, other PML approaches have been suggested and applied successfully ([10,18–22]). However, it appears that no unique PML approach exists. In particular, it is not straightforward and uniquely defined how to choose the PML key parameters, namely, thickness, boundary condition, and stretching function. In most studies, these parameters are determined by trial and error. In this section, we try to resolve such issues by utilizing the layer stiffness matrix in an analytical fashion. We focus on two PML parameters: thickness and boundary condition.

The thickness (h_{PML}) of PML domain should be large enough to prevent wave reflection back into the main computational domain. However, it should not be too large either, because it will require high computational effort in the spatial discretization. Here, we derive an optimal PML thickness (h_{PML}) by comparing the exact stiffness for an SH half space and the exact layer stiffness for an SH layer. Through this case, we also investigate the effect of the boundary condition of the PML domain.

The linear system of equations for a VTI layer subjected to SH wave motion is given in the form:

$$\begin{Bmatrix} p_1 \\ p_2 \end{Bmatrix} = kG_t \frac{\overline{k}_{z3}}{\sinh k\overline{k}_{z3}h} \begin{Bmatrix} \cosh k\overline{k}_{z3}h & -1 \\ -1 & \cosh k\overline{k}_{z3}h \end{Bmatrix} \begin{Bmatrix} u_1 \\ u_2 \end{Bmatrix} \tag{46}$$

and the exact stiffness for the VTI continuum for a half-space is of the form:

$$K_{half\,space,\,exact} = kG_t \sqrt{\left(\frac{C_s}{C_{st}}\right)^2 - \left(\frac{\omega}{kC_{st}}\right)^2} = kG_t \overline{k}_{z3} \tag{47}$$

which is either pure real or pure imaginary, depending on wavenumber k, unless damping is introduced.

In the following, we try to represent the exact half-space stiffness by means of the continuum layer matrix and choosing appropriate thickness (h_{PML}). To this end, we could impose one of the two boundary conditions, namely, Dirichlet or Neumann condition at the bottom of the continuum layer. For the former, we impose the boundary condition of $u_2 = 0$. For the latter, we impose the boundary condition of $p_2 = 0$. Fig. 9 shows schematically the idea of the current approach.

For the Dirichlet boundary condition, we obtain the following relationship from the continuum layer matrix, Eq. (46):

$$p_1 = [G_t k_z \coth k_z h] u_1 \tag{48}$$

where $k_z = k\overline{k}_{z3}$. In order to represent the homogeneous half-space by means of the finite-depth continuum layer, the following equation should be satisfied for all k.

$$G_t k_z \coth k_z h = G_t k_z \tag{49}$$

Alternatively, the following simpler equation should be solved.

$$\coth k_z h = 1 \tag{50}$$

If the layer or half-space doesn't have any damping, the parameter k_z is either purely real or purely imaginary. When k_z is real, the real-valued thickness of $h \geq \pi/k_z$ satisfies $\coth hk_z = 1$ (see the solid curve in Fig. 10). On the other hand, when k_z is imaginary, that is, $k_z = i\beta_z$ with β_z being real-valued, there is no real-valued h that can satisfy $\coth i\beta_z h = 1$. However, if we can assume the thickness as a pure imaginary value, i.e. $h = i\eta$ with η being real-valued, then $\coth i\beta_z i\eta = -\coth \beta_z \eta$. Finally, by increasing the absolute value of η in the negative direction, i.e. $-\eta \geq \pi/\beta_z$, we can satisfy the condition $-\coth \beta_z \eta = 1$ (see the dashed curve in Fig. 10). In summary, we can conclude the following conditions for the thicknesses h and η:

$$h \geq \pi/k_z \tag{51a}$$

$$-\eta \geq \pi/\beta_z \tag{51b}$$

However, we need to consider simultaneously both cases of k_z being real and imaginary. So, we propose the following complex-valued PML thickness (h_{PML}):

$$h_{PML.SH} = \frac{\overline{\lambda}_z}{2}\left(1 - i\right) \tag{52}$$

where $\overline{\lambda}_z \geq 2\pi/|k_z|$ or $2\pi/|\beta_z|$. While the complex-valued stretching for the PML technique is well known, we demonstrate here its necessity through a solid theoretical framework of the stiffness matrix. Fig. 11 shows the performance of this complex-valued thickness by calculating the function $\coth(hk_z)$. It is illustrated that the complex-valued thickness performs very well when the above condition in Eq. (52) is satisfied.

For the Neumann boundary condition of $p_2 = 0$, we can simplify the layer stiffness matrix and obtain the following equation.

$$p_1 = [G_t k_z \tanh k_z h] u_1 \tag{53}$$

This case involves tangent hyperbolic function instead of cotangent hyperbolic function. The behaviors of the two functions are quite similar, except for the small absolute values of argument ($|k_z h| < \pi$), as shown in Fig. 12 and Fig. 13. Therefore, $|hk_z|$ for the Neumann condition should also be no smaller than π, as found out in the Dirichlet boundary condition case, and it is not necessary to repeat the detailed analysis for the Neumann boundary condition. It is expected that the two boundary conditions do not show any difference as long as $|hk_z| \geq \pi$.

The complex-valued thickness chosen above is dependent not only on the frequency $\omega = 2\pi f$ but also on the horizontal (or radial) wavenumber k. This in turn implies that for a given frequency, the thickness is dependent on the wave propagation direction. Consequently, when the wave propagates almost horizontally, i.e. $k \to \omega/C_s$ (for both isotropic and VTI cases), the thickness should be chosen to approach infinity, because the vertical wavelength (λ_z) does so. This can potentially be problematic in spatially-discretized numerical methods (e.g. TLM). However, this problem happens only when the half-space does not have any damping. If the half-space has even a small damping, the vertical wavelength never approaches infinity as $k \to \omega/C_s$. Fig. 14 plots the dimensionless vertical wavenumber $k_z/(\omega/C_s)$ versus the dimensionless horizontal wavenumber $k/(\omega/C_s)$ in terms of both the real and imaginary parts for damping ratio $\xi = 0.01$. The figure shows that the vertical wavenumber never becomes zeros, meaning that the vertical wavelength λ_z is always bounded. Also, note that the magnitude of complex-valued $k_z/(\omega/C_s)$ is minimum at $k/(\omega/C_S) = 1$. Then, it naturally follows that the wavelength is maximum when $k = \omega/C_s$. Fig. 15 plots the dimensionless vertical wavenumber $k_z/(\omega/C_S)$ versus the damping ratio ξ with fixing the horizontal wavenumber $k = \omega/C_S$ indicating that even with a very small damping, the vertical wavenumber is never zero.
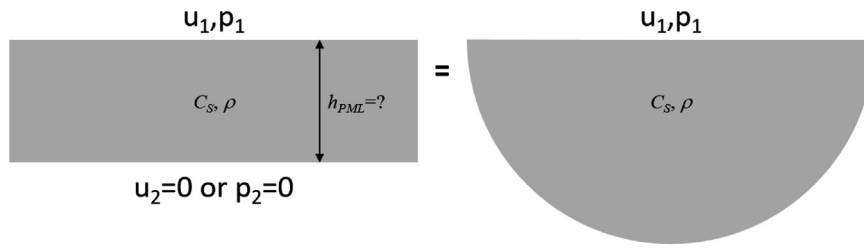
Fig. 9. Sketch of proposed PML approach, representing the exact half-space stiffness (right) by means of the continuum layer matrix and choosing appropriate thickness (left).
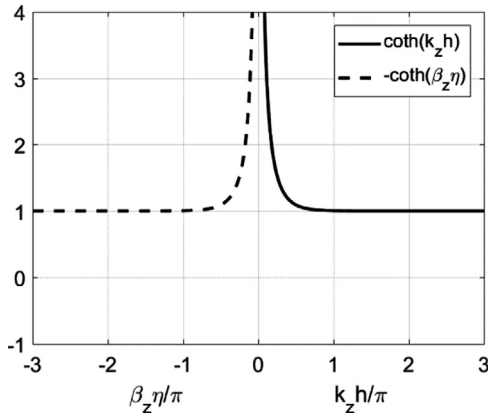

Fig. 10. $\coth(k_z h)$ versus $k_z h/\pi$ (solid, $+$ axis) and $-\coth(\beta_z \eta)$ versus $\beta_z h/\pi$ (dashed, $-$ axis).
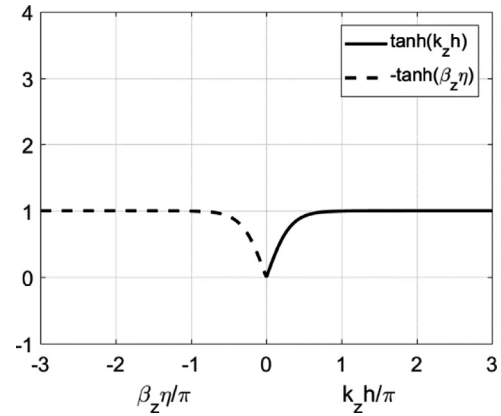

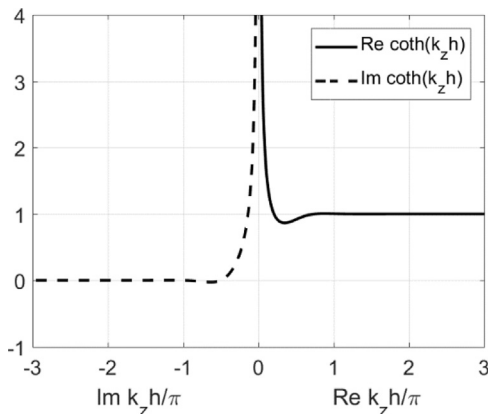**Fig. 12.** $\tanh(k_z h)$ versus $k_z h/\pi$ (solid, $+$ axis) and $-\tanh(\beta_z \eta)$ versus $\beta_z h/\pi$ (dashed, $-$ axis).

Fig. 11. $\coth(k_z h)$ versus real part of $k_z h/\pi$ (solid, $+$ axis) and versus imaginary part of $k_z h/\pi$ (dashed, $-$ axis).
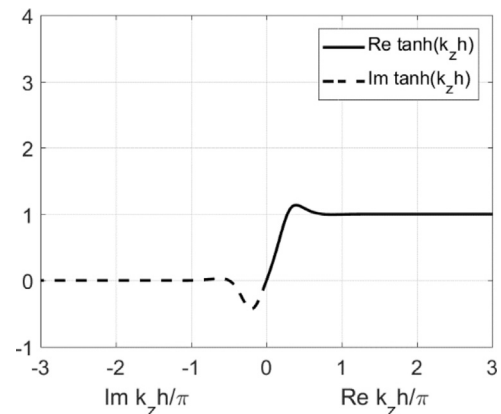

Fig. 13. $\tanh(k_z h)$ versus real part of $k_z h/\pi$ (solid, $+$ axis) and versus imaginary part of $k_z h/\pi$ (dashed, $-$ axis).

Finally, Fig. 16 plots the dimensionless vertical wavelength λ_z/λ_S versus damping ratio ξ, again with fixing the horizontal wavenumber $k = \omega/C_S$ (i.e. when λ_z is maximum). It is noted that with a small damping, the vertical wavelength λ_z is always finite, which in turn means that the PML thickness can also be finite. Fig. 16 shows that for most practical applications where $0.01 \le \xi$ the vertical wavelength λ_z is less than $4\lambda_S$. This implies that $\bar{\lambda}_z$ in Eq. (53) should be no shorter than $4\lambda_S$. When $h_{PML,SH}$ satisfies the above condition, it can be applied to incident wave propagation at any angle.

For the P-SV wave case, we can apply the same logic as presented above, except that we replace λ_s by λ_P; that is,

$$|h_{PML,SVP}| \ge |2\lambda_P(1 - i)| \tag{54}$$

which is relevant for the P-wave damping ratio $\xi_P = 0.01$. So far we have derived an optimal PML thicknesses for the SH and P-SV wave cases, whose amplitude should be larger than $|2 \times \text{wavelength} \times (1 - i)|$. So far, the PML application is discussed in the context of the thin-
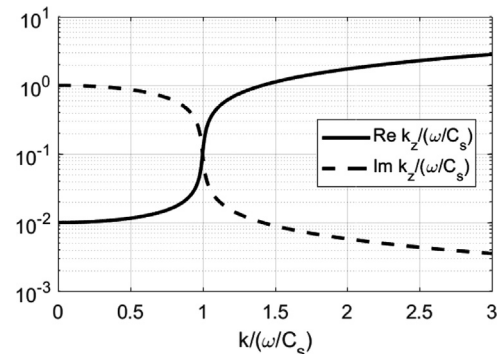

Fig. 14. Dimensionless vertical wavenumber $k_z/(\omega/C_s)$ versus dimensionless horizontal wavenumber $k/(\omega/C_s)$ in terms of both real and imaginary parts for damping ratio $\xi = 0.01$.
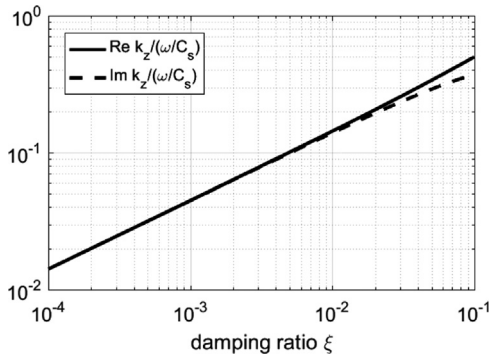
Fig. 15. Dimensionless vertical wavenumber $k_z/(\omega/C_S)$ versus damping ratio ξ with setting $k = \omega/C_S$.
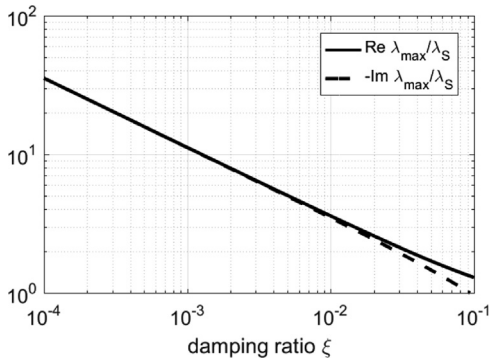

Fig. 16. Dimensionless vertical wavelength λ_z/λ_S versus damping ratio ξ with setting $k = \omega/C_S$.

layer method (TLM) in which the spatial domain is discretized in the vertical direction [10]. However, the concept can be applied to 2D/3D spatial-discretization methods such as finite difference and finite element and finite volume (See Section 7.1).

In addition to implementation in discrete solutions, such as finite element, the continuum PML of complex-valued thickness h_{PML}, described above, can be useful also for analytical solution for simulating an infinite domain. More specifically, it may avoid the need for calculation of the branch-cut integrals in the course of the associated wavenumber contour integration (i.e. Cauchy integration). The reason is that the kernels, i.e. Green's functions, for a finite thickness layer in the wavenumber-frequency domain are always *even* functions with respect to the dimensionless vertical wavenumbers $\overline{k}_{z1}$, $\overline{k}_{z2}$ or $\overline{k}_{z3}$, which in turn make the kernels branch-cut free [9]. This can be easily observed by inspecting, for example, the two stiffness matrices of a layer and a half-space in Eqs. (46) and (47). In Eq. (46), the two terms of sinh $k\overline{k}_{z3}h$ and $k\overline{k}_{z3}$ are located together in the coefficient term, each of which is an *odd* function with respect to $\overline{k}_{z3}$. Since they are in the same coefficient term, i.e. in denominator and numerator, respectively, the whole coefficient term becomes an *even* function with respect to $\overline{k}_{z3}$, hence, branch-cut free. On the other hand, $\overline{k}_{z3}$ exists alone in Eq. (47), resulting in a branch point at $\overline{k}_{z3} = 0$ and requiring the branch-cut integral in the context of the contour integration in order to transform the wavenumber-domain response to the spatial-domain response.

7.1. Homogeneous stratum subjected to SH line load

A simple canonical problem is considered in this section to demonstrate the performance of the PML parameter (h_{PML}) suggested here. For the PML application, we use the finite element approach based on *COMSOL Multiphysics™* (commercial FE software), in which we can easily implement the PML technique developed earlier. The canonical problem is a homogeneous stratum of thickness H that is subjected

to boundary conditions of fixed-displacement at the bottom and stress free at the top surface, and excited by a harmonic SH line load at the top surface. The exact analytical solution for an isotropic stratum is available in the modal superposition form [9]. By following the same approach as in [9], the exact analytical solution for the VTI stratum can be derived and given as

$$\nu(x, z, f) = \frac{P(f)}{iG_t b^2 H} \sum_{j=1}^{\infty} \phi(z)\phi(z_s)\frac{e^{-k_j|x|}}{k_j} \quad \text{(displacement)} \tag{55a}$$

$$k_j = b^{-1}\sqrt{(2\pi f)^2 - [(j-1/2)\pi/H]^2} \quad \text{(eigen-wavenumber)} \tag{55b}$$

$$\phi(z) = \cos(j-1/2)\pi z/H \quad \text{(mode shape)} \tag{55c}$$

We consider an SH line load of $P(f) = 1$ N and $f = 10$ Hz, and the mechanical properties of the stratum are set to $\rho = 1500$ kg/m^3, $C_{st} = 1000$ m/s, $\xi = 0.01$, $H = 250$ m. In addition, we consider the isotropic stratum as well as the VTI in order to compare the two cases. Finally, we assume $z = z_s = 0$.

For the selected frequency of 10 Hz, the wavelength $\lambda_s (= C_{st}/f)$ is 100 m. Following the PML approach suggested earlier, we should use h_{PML} of no shorter than 200 m. Fig. 17(a) and (b) depicts the finite element model and the mesh used in the analysis. Triangular quadratic elements of ca. 25 m size are used in the entire model including the PML domains on the sides. It is noted that the PML domain size in Fig. 17(a) is the same as h_{PML}. This means that we are applying no stretching function for the PML domains so that we can evaluate the performance solely of h_{PML} suggested earlier. Efficient stretching functions, (e.g. [10,22]), can be chosen, which can further reduce the computational effort. Fig. 17 (c) and (d) show the computed responses for the isotropic and anisotropic strata, respectively, both in terms of real (solid) and imaginary (dashed) components. In addition, the related exact analytical solutions (real: dashed-dotted; imaginary: dotted) are plotted for comparison. It is clearly observed that the PML approach suggested in this study performs very well and produces highly accurate results even near the interface between the main and PML domains (i.e. $x = 0$ and 800 m). It should be noticed that the agreement between the finite element and Exact solutions near the source point $x = 250$ m is poor, as expected, because of the mesh size applied.

8. Summary and conclusion

In this study, we introduce and discuss features and improvements of the stiffness matrix method developed in [1] that may enhance the applicability and flexibility of the method. Several numerical examples are provided to support the improvements and features. First, we introduce the acoustic layer stiffness matrices by means of three different formulations in terms of vertical displacement, velocity potential and nodal pressure, respectively. The latter two are easy for implementing air-gun source, while the first one is straightforward to apply a vertical disk load on seabed or within the water layer. Secondly, the soil stiffness matrices for the vertically transverse isotropic (VTI) layer are derived for both P-SV and SH wave modes. The structure of the VTI soil layer stiffness matrices is constructed in the same fashion as for the isotropic soil layer and such that the stiffness matrix for the isotropic case can be recovered by setting the anisotropy factors equal to 1. Thirdly, in order to simulate wave motions subjected to injected (air) volume or dislocation/slip at the interface of two layers, we formulate a technique where the displacement discontinuity can be implemented. Finally, by means of the continuum stiffness matrices we derive the key parameter of PML (thickness, h_{PML}) that can be used in discrete numerical approaches (e.g. FEM, FDM, TLM). We also discuss how the continuum PML can be useful for the contour integration over the complex wavenumber domain, eliminating the need for the branch-cut integral, in the context of the wavenumber integration from the wavenumber to spatial domain.
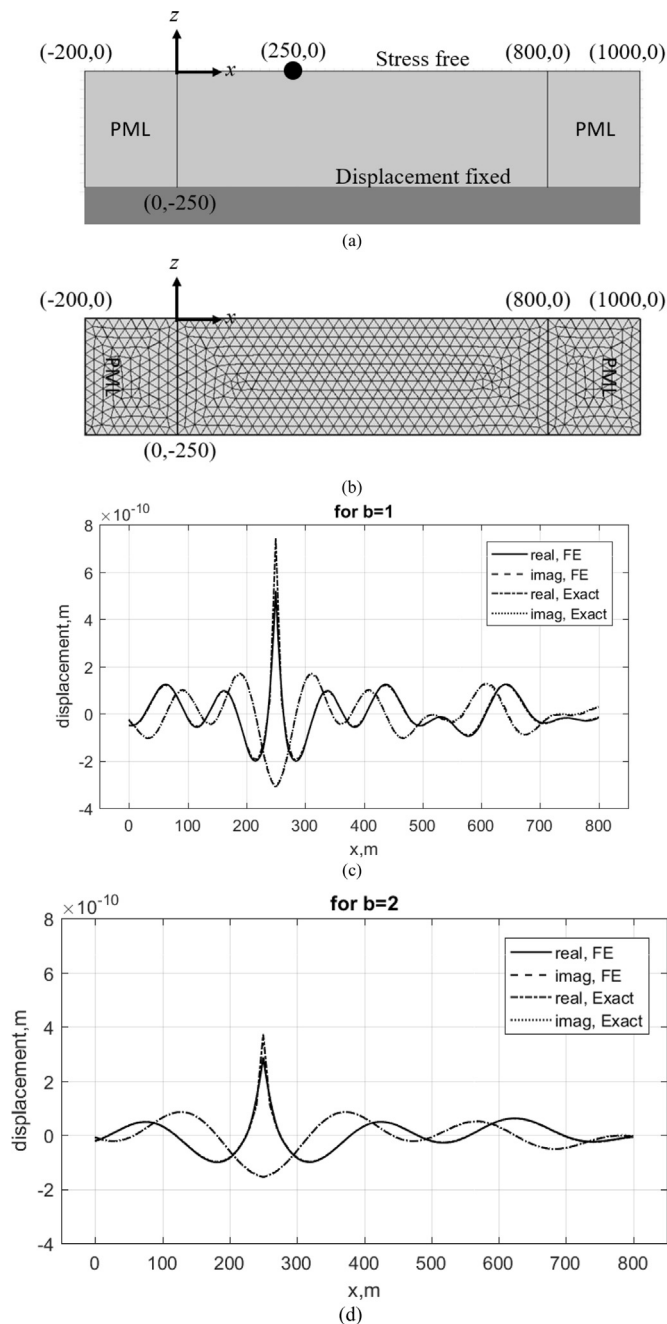
Fig. 17. (a) finite element model description of a 250 m-thick homogeneous stratum (with 800 m-long main domain in the middle and two 200 m-long PML domains at the sides) subjected to SH line load applied at (250,0) (black circle); (b) triangular finite element mesh; (c) displacement along top surface of isotropic stratum with $b = 1$ calculated by both finite element and exact solutions; (d) displacement along top surface of anisotropic stratum with $b = 2$ calculated by both solutions.

References

[1] Kausel E, Roësset JM. Stiffness matrices for layered soils. Bull Seismol Soc Am 1981;71:1743–61.
[2] Wang Y, Rajapakse RKND. An exact stiffness method for elastodynamics of a layered orthotropic half-space. J Appl Mech 1994;61:339–47.
[3] Rokhlin SI, Wang L. Stable recursive algorithm for elastic wave propagation in layered anisotropic media: stiffness matrix method. J Acoust Soc Am 2002;112:822–34.
[4] Tan EL. Stiffness matrix method with improved efficiency for elastic wave propagation in layered anisotropic media. J Acoust Soc Am 2005;118:3400–3.
[5] Roësset JM, Wright SG, Sedighi-Manesh M. Hovem JM, Richardson MD, Stoll RD, editors. Analytical investigation of seismic surface waves in the seafloor, Shear Waves in Marine Sediments. Kluwer Academic Publishers; 1991.
[6] Kaynia AM, Kausel E, Madshus CM. Impedances of Underwater Rigid Square Foundations. Proceedings ASCE Spec. Conference Geotech. Earthquake Engng, Seattle, WA, USA, 1283 − 1293; 1998.
[7] Kausel E, Peek R. Dynamic loads in the interior of a layered stratum: an explicit solution. Bull Seismol Soc Am 1982;72:1459–81.
[8] Lotfi V, Roësset JM, Tassoulas JL. A technique for the analysis of the response of dams to earthquakes. Earthq Eng Struct Dyn 1987;15:463–90.
[9] Park J. Wave motion in finite and infinite media using the Thin-Layer Method [Sc.D. Thesis]. Department of Civil and Environmental Engineering, MIT; 2002.
[10] Barbosa JM, Park J, Kausel E. Perfectly matched layers in the thin layer method. J Comput Methods Appl Mech Eng 2012;217–220:262–74.
[11] Wong HL, Luco JE. Tables of impedance functions for square foundations on layered media. Soil Dyn Earthq Engng 1985;4(2):64–81.
[12] Wong HL, Luco JE. Dynamic response of rigid foundations of arbitrary shape. Earth Engng Str Dyn 1976;4:579–87.
[13] Fryer GJ, Frazer LN. Seismic waves in stratified anisotropic media. Geophys J R Astron Soc 1984;78:691–710.
[14] Crouch SL, Starfield AM. Boundary element method in solid mechanics. London: George Allen & Unwin; 1983.
[15] Bucinskas P, Andersen LV. Semi-analytical approach to modelling the dynamic behaviour of soil excited by embedded foundations, X International Conference on Structural Dynamics, EURODYN 2017, Procedia Engineering, 199; 2017. p. 2621–2626.
[16] Lysmer J, Tabatabaie M, Tajirian FF, Vahduni S, Ostradan F. SASSI A System for Analysis of Soil Structure Interaction, UCB/GT-81/02 Geotech. Eng., U.C. Berkeley; 1981.
[17] Bérenger JP. A perfectly matched layer for the absorption of electromagnetic waves. J Comput Phys Vol 1994;114:185–200.
[18] Collino F, Tsogka C. Application of the perfectly matched absorbing layer model to the linear elastodynamic problem in anisotropic heterogeneous media. GEOPHYSICS 2001;66:294–307.
[19] Basu U, Chopra AK. Perfectly matched layers for time-harmonic elastodynamics of unbounded domains: theory and finite-element implementation. Comput Methods Appl Mech Eng 2003;192:1337–75.
[20] Festa G, Nielsen S. PML absorbing boundaries. Bull Seismol Soc Am 2003;93:891–903.
[21] Guddati MN, Lim KW. Continued fraction absorbing boundary conditions for convex polygonal domains. Int J Numer Methods Eng 2005;66:949–77.
[22] Park J, Kaynia AM. FE simulation of steady state wave motion in solids combined with a PML approach [X International Conference on Structural Dynamics, EURODYN 2017]. Procedia Eng 2017;199(2017):1556–61.